Ulrich Häussler-Combe

Computational Structural Concrete

Theory and Applications

- guidance for the direct application of numerical methods to concrete structures
- the book is suitable for beginners in the profession and for practicing engineers
- state of the art concrete material models are presented

Basic concepts of numerical methods in particular the FEM are summarized. The theory is explicated for structural concrete parts like beams plates, slabs and shells. Thus the operation of complex software is made transparent incl. opportunities and pitfalls. With 42 examples.

ORDER

+49 (0)30 470 31–236
marketing@ernst-und-sohn.de
www.ernst-und-sohn.de/en/3310

* All book prices inclusive VAT.

WILEY

Ernst & Sohn
A Wiley Brand

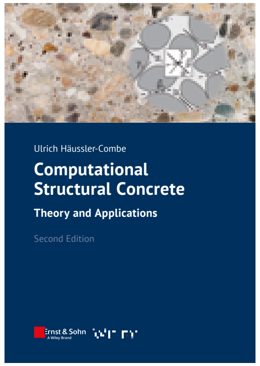

prelim. fig.

2., enlarged and improved Edition · 10 / 2022 · approx. 448 pages · approx. 158 figures · 11 tables

Softcover
ISBN 978-3-433-03310-4 approx. **€ 79***

eBundle (Print + ePDF)
ISBN 978-3-433-30001-5 approx. **€ 99***

Available for pre-order.

WILEY Ernst & Sohn
A Wiley Brand

ABOUT THE BOOK

Concrete is by far the most used building material due to its advantages: it is shapeable cost-effective and available everywhere. Combined with reinforcement it provides an immense bandwidth of properties and may be customized for a huge range of purposes. Thus concrete isthe building material of the 20th century. To be the building material of the 21th century its sustainability has to move into focus. Reinforced concrete structures have to be designed expending less material whereby their load carrying potential has to be fully utilized. Computational methods such as Finite Element Method (FEM) provide essential tools to reach the goal. In combination with experimental validation they enable a deeper understanding of load carrying mechanisms. A more realistic estimation of ultimate and serviceability limit states can be reached compared to traditional approaches. This allows for a significantly improved utilization of construction materials and a broader horizon for innovative structural designs opens up.
However sophisticated computational methods are usually provided as black boxes. Data is fed in the output is accepted as it is but anunderstanding of the steps in between is often rudimentary. This has the risk of misinterpretations not tosay invalid results compared to initial problem definitions. The risk is in particular high for nonlinear problems. As a composite material reinforced concrete exhibits nonlinear behaviour in its limit states caused byinteraction of concrete and reinforcement via bond and the nonlinear properties of the components. Its cracking is a regular behaviour. The book aims to make the mechanisms of reinforced concrete transparent from the perspective of numerical methods. In this way black boxes should also become transparent.
Appropriate methods are described for beams plates, slabs and shells regarding quasi-statics and dynamics. Concrete creeping temperature effects prestressing, large displacements are treated as examples. State of the art concrete material models are presented. Both the opportunities and the pitfalls of numerical methods are shown. Theory is illustrated by a variety of examples. Most of them are performed with the ConFem software package implemented in Python and available under open-source conditions.

ORDER

Quantity	ISBN / Order-No.	Title	Price €
	978-3-433-03310-4	Computational Structural Concrete [...]	approx. € 79*
	978-3-433-30001-5	Computational Structural Concrete (Print + ePDF)	approx. € 99*

☐ Private ◯ Business

Please send your order to:
marketing@ernst-und-sohn.de

Company Abteilung

VAT-ID

Name

Phone

Fax

Street No.

Zip code / City / Country

E-Mail

www.ernst-und-sohn.de/en/3310

Date Signature

. As of 8/2022

Preface

This book grew out of lectures that the author gave at the Technische Universität Dresden. These lectures were entitled "Computational Methods for Reinforced Concrete Structures" and "Design of Reinforced Concrete Structures." Reinforced concrete is a composite of concrete and reinforcement connected by bond. Bond is a key item for the behaviour of the composite, which utilises the compressive strength of concrete and the tensile strength of reinforcement while allowing for controlled crack formation. This makes reinforced concrete unique compared to other construction materials such as steel, wood, glass, masonry, plastic materials, fibre reinforced plastics, geomaterials, etc. The theory and use of reinforced concrete in structures falls in the area of structural concrete.

Numerical methods like the finite element method, on the other hand, basically allow for a realistic computation of the behaviour of all types of structures. But the implementations are generally presented as black boxes in the view of the users. Input is fed in and the output has to be trusted. The assumptions and methods in-between are not transparent. This book aims to provide transparency with special attention being paid to the unique properties of reinforced concrete structures. Corresponding methods are described with their potentials and limitations while integrating them into the larger framework of computational mechanics connected to reinforced concrete. This is aimed at advanced students of civil and mechanical engineering, academic teachers, designing and supervising engineers involved in complex problems of structural concrete, and researchers and software developers interested in the broader picture. Most of the methods described are complemented with examples computed with a PYTHON software package developed by the author and coworkers. Program package and example data should be available at https://www.concrete-fem.com. The package exclusively uses the methods described in this book. It is open for discussion with the disclosure of the source code and should give stimulation for alternatives and further developments.

This book represents a fundamental revision of the book COMPUTATIONAL METHODS FOR REINFORCED CONCRETE STRUCTURES, which was published in 2014. In particular, the chapter on multi-axial concrete material laws was expanded, and the topics of crack formation and the regularisation of material laws with strain softening were dealt with in a separate chapter. Thanks are given to the publisher

Ernst & Sohn, Berlin, and in particular to Mrs Claudia Ozimek for the engagement in supporting this work. My education in civil engineering and my professional and academic career were guided by my academic teacher Prof. Dr.-Ing. Dr.-Ing. E.h. Dr. techn. h.c. Josef Eibl[1)], former Head of the Department of Concrete Structures at the Institute of Concrete Structures and Building Materials at the Technische Hochschule Karlsruhe (nowadays KIT – Karlsruhe Institute of Technology). Further thanks are given to former coworkers Patrik Pröchtel, Jens Hartig, Mirko Kitzig, Tino Kühn, Joachim Finzel, Tilo Senckpiel-Peters, Daniel Karl, Ahmad Chihadeh, Ammar Siddig Ali Babiker, Evmorfia Panteki, and Alaleh Sehni for their specific contributions. I deeply appreciate the inspiring and collaborative environment of the Institute of Concrete Structures at the Technische Unversität Dresden, which is directed by Prof. Dr.-Ing. Dr.-Ing. E.h. Manfred Curbach. It was my pleasure to teach and research at this institution. And I have to express my deep gratitude to my wife Caroline for her love and patience.

Dresden, Spring 2022 *Ulrich Häussler-Combe*

1) He passed away in 2018.

Contents

List of Examples

4.8 Prestressing

Prestressing applies lateral redirection forces and normal forces on a beam, see Figure 4.16a. While the redirection forces act against dead and variable loads a moderate normal force may increase the bearing capacity for moments (Example 4.1.3.3, Figure 4.4). But these positive effects require prestressing tendons. A concrete beam and its ordinary reinforcement on the one hand and the tendons with high strength steel on the other hand are regarded as separated structural elements in the following.

We consider the Bernoulli beam. Primarily, the generalised stress $\boldsymbol{\sigma}$ (Eq. 4.60)) is formulated as a function of the generalised strains

$$\boldsymbol{\sigma} = \mathbf{C} \cdot \boldsymbol{\epsilon} \tag{4.162}$$

with, e.g. $\mathbf{C}$ according to Eq. (4.16) or Eq. (4.42). A linear $\mathbf{C}$ is not necessarily required. This concept is extended with respect to prestressing: an additional part is assigned to the generalised stresses resulting from *prestressing tendons*

$$\boldsymbol{\sigma} = \mathbf{C} \cdot \boldsymbol{\epsilon} + \boldsymbol{\sigma}^p \tag{4.163}$$

This additional part $\boldsymbol{\sigma}^p$ depends on the tendon profile

$$\boldsymbol{\sigma}^p = \begin{pmatrix} N^p \\ M^p \end{pmatrix} = -F^p \begin{pmatrix} \cos\alpha_p \\ -z_p \cos\alpha_p \end{pmatrix} \tag{4.164}$$

with the prestressing force F^p, the height coordinate or lever arm z_p of the tendon and the inclination $\alpha_p = \mathrm{d}z_p / \mathrm{d}x$ of the tendon against the beam reference axis, see Figure 4.16b. This may be extended with respect to shear forces in combination with the Timoshenko beam. Using the extended generalised stresses Eq. (4.163) for the internal nodal forces Eq. (4.97) leads to a split

$$\mathbf{f}_e = \int_{L_e} \mathbf{B}^{\mathrm{T}} \cdot \boldsymbol{\sigma}\, \mathrm{d}x = \int_{L_e} \mathbf{B}^{\mathrm{T}} \cdot \mathbf{C} \cdot \boldsymbol{\epsilon}\, \mathrm{d}x + \int_{L_e} \mathbf{B}^{\mathrm{T}} \cdot \boldsymbol{\sigma}^p\, \mathrm{d}x = \mathbf{f}_e^{\epsilon} + \mathbf{f}_e^p \tag{4.165}$$

The part $-\mathbf{f}_e^p$ may be regarded as a further contribution to the load vector (Eq. (2.59)) or external nodal forces. This approach integrates prestressing in the given

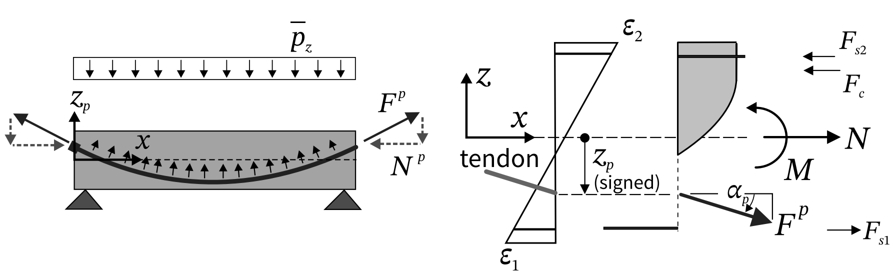

Figure 4.16 (a) Redirection forces from prestressing. (b) Internal forces with prestressing.

framework whereby all procedures but for a part of load evaluation remain unchanged.

An alternative and common view of prestressing of beams is based on Eqs. ($4.49_{2,3}$). We consider the quasi-static case, split internal forces into a part $\bullet^\epsilon$ from beam deformation, a part $\bullet^p$ from prestressing and eliminate shear forces

$$-M^{\epsilon\prime\prime} - M^{p\prime\prime} = \overline{p}_z \tag{4.166}$$

and furthermore Eq. (4.164) is used leading to

$$-M^{\epsilon\prime\prime} = \overline{p}_z + \left(z_p F^p \cos\alpha_p\right)^{\prime\prime} \tag{4.167}$$

A common approximation is $F^p \approx const.$, $\cos\alpha_p \approx 1$ resulting in

$$-M^{\epsilon\prime\prime} = \overline{p}_z + z_p^{\prime\prime} F^p \tag{4.168}$$

wherein $z_p^{\prime\prime} F^p$ is a lateral redirection force in the z-direction from the curvature $z_p^{\prime\prime}$ of the tendon geometry. This term may be seen as an additional lateral loading counteracting the other loadings (Figure 4.16).

Some characteristic properties of prestressing have to be regarded for the evaluation of $\boldsymbol{\sigma}^p$ or $\mathbf{f}^p$, respectively.

- Tendon profile parameters z_p, α_p may vary with the beam coordinate x according to prestressing design.
- The prestressing force may vary due to the loss of prestress from friction of the tendon in a conduit.
- Furthermore, a beam deformation may lead to a change in the tendon profile. Two types have to be considered in this context:
  1. *Unbonded prestressing*: total length of the tendon changes. This leads to a global change of the prestressing force.
  2. *Bonded prestressing*: length of the tendon changes locally to keep the geometric compatibility with the concrete. This leads to locally varying changes in the prestressing force.

Two subsequent stages have to be considered for prestressing:

- *Set-up stage* of prestressing with the prescribed prestressing force F_0^p
  Prestressing is gradually applied at the beam ends through anchors. The value of F_0^p may vary along the longitudinal beam coordinate x due to friction losses. Such losses have to be determined from prescribed friction coefficients and the curvature of the tendon geometry.
- Tendons may be grouted at the end of the set-up stage leading to *post-bonding*. This is generally denoted as bonded prestressing although this is not entirely precise. Grouting is omitted for unbonded prestressing.
- *Service stage* of prestressing with locked anchors
  The prestressing force F_0^p changes into F_p depending on loading and prestressing type.

The tendon geometry plays a key role. It is described for each finite beam element in analogy to the Bernoulli beam trial function (Eq. (4.82)) by

$$z_p = \left[\frac{r^3}{4} - \frac{3r}{4} + \frac{1}{2} \quad \frac{L_e r^3}{8} - \frac{L_e r^2}{8} - \frac{L_e r}{8} + \frac{L_e}{8} \quad -\frac{r^3}{4} + \frac{3r}{4} + \frac{1}{2} \quad \frac{L_e r^3}{8} + \frac{L_e r^2}{8} - \frac{L_e r}{8} - \frac{L_e}{8} \right] \cdot \begin{pmatrix} z_{pI} & \alpha_{pI} & z_{pJ} & \alpha_{pJ} \end{pmatrix}^{\mathrm{T}} \tag{4.169}$$

with the element length L_e and the tendon inclination

$$\alpha_P = \frac{\partial z_p}{\partial x} = \frac{\partial z_p}{\partial r} \frac{\partial r}{\partial x} = z'_p \tag{4.170}$$

Lateral tendon position z_p and inclination α_p at the left-hand and right-hand element nodes are given by z_{pI}, α_{pI} and z_{pJ}, α_{pJ}. The local element coordinate is in the range $-1 \leq r \leq 1$. This approach reproduces $z_p(-1) = z_{pI}$, $z'_p(-1) = \alpha_{pI}$ and $z_p(1) = z_{pJ}$, $z'_p(1) = \alpha_{pJ}$. The geometric length of a tendon within an element e is given by

$$L_e^P = \frac{L_e}{2} \int_{-1}^{1} \sqrt{(x'_p)^2 + (z'_p)^2} \ \mathrm{d}r \tag{4.171}$$

whereby the derivative of the tendon position x_p in the longitudinal direction has also to be regarded. We obtain

$$x'_p = 1 \tag{4.172}$$

for the nominal undeformed tendon geometry and

$$x'_p = 1 + \epsilon \tag{4.173}$$

considering beam deformations with the longitudinal strain ϵ of the reference axis. Furthermore, on the one hand Eq. (4.169) is applied to the nominal undeformed tendon geometry according to design with

$$\begin{pmatrix} z_{pI} & \alpha_{pI} & z_{pJ} & \alpha_{pJ} \end{pmatrix} = \begin{pmatrix} z_{p0I} & \alpha_{p0I} & z_{p0J} & \alpha_{p0J} \end{pmatrix} \tag{4.174}$$

with prescribed values $z_{p0I}, \alpha_{p0I}, z_{p0J}, \alpha_{p0J}$. On the other hand, Eq. (4.169) gives the tendon geometry considering beam deformations with

$$\begin{pmatrix} z_{pI} & \alpha_{pI} & z_{pJ} & \alpha_{pJ} \end{pmatrix} = \begin{pmatrix} z_{p0I} + w_I & \alpha_{p0I} + \phi_I & z_{p0J} + w_J & \alpha_{p0J} + \phi_J \end{pmatrix} \tag{4.175}$$

with the beam nodal displacements w_I, ϕ_I, w_J, ϕ_J. This yields z'_p from Eq. (4.169) according to Eq. (4.82$_2$). The Eq. (4.171) has to be integrated numerically for each element, e.g. with a Gauss integration (Section 2.7). The total length L^P of a tendon is given by adding all element contributions.

Regarding prestressing *without bond* the tendon length can be determined separately with a value L_0^P for the set-up stage and with a value L^P for the service stage whereby Eq. (4.175) is used with the actually calculated nodal displacements for each stage. This has a side effect.

Strains of unbonded tendons do not follow the Bernoulli–Navier hypothesis (Section 4.1.1).

The prestressing force is prescribed with F_0^p for the set-up stage and is determined with

$$F^p = \frac{L^P}{L_0^P} F_0^p \tag{4.176}$$

in the service stage of prestressing.

Regarding prestressing with *post-bonding* a tendon gets a *local* elongation after locking of prestressing anchors and grouting due to bond between tendons and concrete. This local elongation is ruled by the beam deformation kinematics (Eq. (4.5)) and the additional strain of the tendon is given by

$$\Delta\epsilon_p(x) = \Delta\epsilon(x) - z_p\,\Delta\kappa(x) \tag{4.177}$$

with the difference $\Delta\epsilon$, $\Delta\kappa$ of generalised strains between set-up and service stage whereby varying along the beam axis.

Strains of post-bonded tendons follow the Bernoulli–Navier hypothesis during the service stage although not during the set-up stage.

This leads to a prestressing force

$$F^p(x) = F_0^p + E_p A_p\,\Delta\epsilon_p(x) \tag{4.178}$$

in the service stage with Young's modulus E_p of the prestressing steel – elastic behaviour is assumed to simplify – and the cross-sectional area A_p of tendons.

Finally, internal prestressing forces contributing to loadings are determined using Eq. (4.164). A loading from prestressing distinguishes from self weight, service load, temperature as it depends on displacements and yields a nonlinear load contribution. But the computations show that F^p and F_0^p generally do not differ by large amounts. Thus, the particular procedures concerning prestressing can be summarised with

- define the tendon geometry and prestressing force,
- compute internal forces from prestressing,
- compute nodal forces from prestressing and apply as loads,
- compute system reaction,
- iterate if necessary to consider a change in prestressing forces

which seamlessly fits into the incrementally iterative approach (Section 2.8.2). The application is demonstrated with the following example.

Example 4.6: Prestressed RC beam

We refer to Example 4.2 with basically the same system, but the span is doubled to $L = 10\,\text{m}$. Thus, load bearing capacity is strongly reduced. Prestressing is used to maintain this capacity. The relevant system parameters are as follows:

- A concrete cross-section $b = 0.2$, $h = 0.4$, a compressive strength $f_{cd} = 38\,\text{MN/m}^2$ and a lower and upper reinforcement $A_{s1} = A_{s2} = 12.57\,\text{cm}^2$, $d_1 = d_2 = 5\,\text{cm}$ yield an ultimate bending moment $M_u \approx 0.20\,\text{MNm}$ with $N = 0$ (Example 4.1, Figure 4.4). This corresponds to an uniform loading $q_u = 8M_u/L^2 = 15.2\,\text{kN/m}$ which should be increased by prestressing.
- A nominal uniform concrete prestressing stress of $\sigma_{c0} = -10\,\text{MN/m}^2$ is chosen in a first approach leading to $F_0^p = 0.8\,\text{MN}$. The nominal tendon geometry of the whole beam is given by a parabola starting and ending in the centre line with a downward catenary h_p. This is described by

$$z_p = 4h_p\left(\frac{x^2}{L^2} - \frac{x}{L}\right) \tag{4.179}$$

  A value $h_p = 0.15\,\text{m}$ is chosen in this example.
- Prestressing tendon and steel properties are chosen with cross-sectional area $A_p = 6\,\text{cm}^2$, elastic limit $f_{p0,1} = 1600\,\text{MN/m}^2$, strength $f_p = 1800\,\text{MN/m}^2$, Young's modulus $E_p = 200\,000\,\text{MN/m}^2$, nominal initial steel stress $\sigma_0^p = 1333\,\text{MN/m}^2$ with a strain $\epsilon_0^p = 6.67\,‰$.
- A dead load is assumed with $q = 5\,\text{kN/m}$.

Loading is applied in two steps: (1) set-up of prestressing and dead load, (2) locking of prestressing and additional application of a service load $q_p = 25\,\text{kN/m}$. Frictional losses are neglected to simplify this example. Both cases – prestressing with and without bond – are alternatively regarded for the service stage of prestressing. The solution method is incrementally iterative with Newton–Raphson iteration within increments. This leads to the following results for prestressing *without* bond:

- The computed increase in prestressing force after load step 2 according to Eq. (4.176) is minimal with $F^p/F_0^p = 1.002$. This results from the low ratio $h_p/L = 1/67$.
- For the computed mid-span displacements, see Figure 4.17a. The deflection starts with an uplift during application of prestressing. The final mid-span deflection in load step 2 is quite large with 0.107 m ($\approx 1/90$ of the span), but the load-carrying capacity is not yet exhausted with an upper mid-span concrete compressive strain of $-2.0\,‰$ (limit strain is $-3.5\,‰$). Serviceability is presumably not given without further provisions due to the high slenderness (1/25).
- For the bending moment M_c in the RC cross-section only see Figure 4.18a. The total moment from the dead load and the service load is $M_q = 0.03 \cdot 10^2/8 = 0.375\,\text{MNm}$. The computed RC mid-span contribution is $M_c = 0.255$ and the contribution from prestressing $M_p = 0.120$. The increased RC moment compared to the initial estimation results from the compressive normal force.

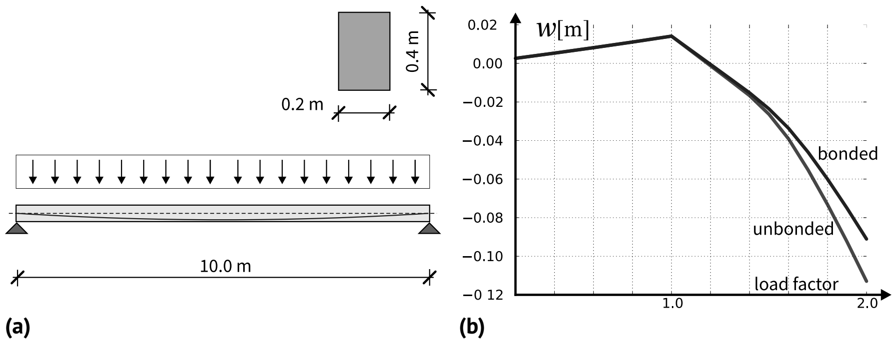

Figure 4.17 Example 4.6. (a) System. (b) Mid-span load–deflection curve.

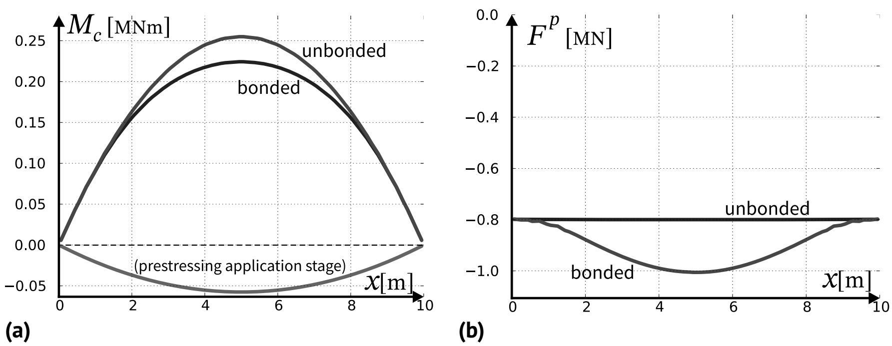

Figure 4.18 Example 4.6. Final stage. (a) RC bending moment M_c. (b) Prestressing force F^p.

Furthermore, the results for prestressing *with* post-bonding:

- The tendon gets a local additional strain due to the locally varying deformation of the beam (Eq. (4.177)). This leads to an additional prestressing force F^p, see Eq. (4.178) and Figure 4.18b, and to a higher contribution of prestressing to the load bearing capacity whereby reducing concrete demand.
- More significant results are given with the final mid-span deflection reduced to 0.086 m (Figure 4.17b) compared to the unbonded case, the RC moment contribution reduced to $M_c = 0.220$ (Figure 4.18a) and the prestressing moment contribution increased to $M_p = 0.155$.

Prestressing roughly leads to a doubling of ultimate limit loads in this example. Aspects of serviceability have to be treated separately. The comparison between prestressing with and without bond in this example is somehow academic, as in practice prestressing with bond is exposed to more non-mechanical effects which might lead to some restrictions to fully utilise the load carrying capacities of the prestressing steel. Details are ruled in codes.

Finally, the uniaxial stress–strain relations are derived for the two material symmetry directions. The 1-direction has $\sigma_{22} = 0$, leading to

$$\sigma_{11} = E_1\, \epsilon_{11}\,, \quad \epsilon_{22} = -\frac{\overline{\nu}}{\sqrt{E_1 E_2}}\, \sigma_{11} \tag{6.35}$$

With given values for σ_{11}, ϵ_{11}, ϵ_{22} from a test A, two equations are given for three unknowns E_1, E_2, $\overline{\nu}$. The 2-direction has $\sigma_{11} = 0$ leading to

$$\sigma_{22} = E_2\, \epsilon_{22}\,, \quad \epsilon_{11} = -\frac{\overline{\nu}}{\sqrt{E_1 E_2}}\, \sigma_{22} \tag{6.36}$$

With given values for σ_{22}, ϵ_{22}, ϵ_{11} from a test B – strains from test A and test B are not the same – two further equations are given for the unknown material parameters. Thus, the set of four equations (6.35) and (6.36) is overdetermined for the unknowns E_1, E_2, $\overline{\nu}$. A best fit may be found with a least squares approach (Appendix E, Eqs. (E.2)–(E.6)).

6.4 Nonlinear Material Behaviour

6.4.1 Tangential Stiffness

With respect to the uniaxial case, nonlinear material behaviour of concrete is characterised by a decreasing tangential material stiffness (Figure 3.1). This property is transferred to the multi-axial case. A general formulation of nonlinear material behaviour is given by Eq. (6.12)

$$\dot{\boldsymbol{\sigma}} = \mathbf{C}_T \cdot \dot{\boldsymbol{\epsilon}} \tag{6.37}$$

With respect to the initial behaviour of previously unloaded concrete, it can be assumed that it initially behaves as a linear elastic isotropic material. The initial tangential material stiffness matrix $\mathbf{C}_T$ is given according to Eq. (6.23). Values for the initial Young's modulus E_c and the initial Poisson's ν ratio depending on concrete grade are given by EN 1992-1-1 (2004, 3.1.3), CEB-FIP2 (2012, 5.1.7). But a tangential stiffness matrix $\mathbf{C}_T$ is subject to change after the initial state and may depend on stress $\boldsymbol{\sigma}$, strain $\boldsymbol{\epsilon}$ and internal state variables $\boldsymbol{\kappa}$

$$\mathbf{C}_T = \mathbf{C}_T(\boldsymbol{\sigma}, \boldsymbol{\epsilon}, \boldsymbol{\kappa}) \tag{6.38}$$

Internal state variables $\boldsymbol{\kappa}$ comprise a loading history. They are necessary, as an actual state $\boldsymbol{\sigma}, \boldsymbol{\epsilon}$ may lead to different responses $\dot{\boldsymbol{\sigma}}$ for different loading histories with a given $\dot{\boldsymbol{\epsilon}}$. Internal state variables require *evolution laws*

$$\dot{\boldsymbol{\kappa}} = \mathcal{F}(\boldsymbol{\sigma}, \boldsymbol{\epsilon}, \boldsymbol{\kappa}) \tag{6.39}$$

describing their rates depending on stress, strain, and values of internal state variables.

Aspects of isotropy and anisotropy as were described in Section 6.3 are also an issue for nonlinear behaviour. Isotropic nonlinear behaviour is characterised in the same way as was formulated in Section 6.3.1. The previous reasoning regarding $\boldsymbol{\sigma}$, $\boldsymbol{\epsilon}$ in the same way applies to rates $\dot{\boldsymbol{\sigma}}$, $\dot{\boldsymbol{\epsilon}}$, leading the same conclusion about the principal directions of the stress and strain rates and to the same restrictions for the coefficients of an isotropic tangential material stiffness $\mathbf{C}_T$

A *nonlinear isotropic* material behaves in the same way in every action direction. Principal directions of stress *increments* coincide with principal directions of strain *increments* for a given material state. The principal stress increments have the same values for all principal strain directions with given strain increment values.

In analogy to Eq. (6.20), an isotropic tangential material stiffness matrix obeys a relation

$$\mathbf{C}_T = \mathbf{Q}^{\mathrm{T}} \cdot \mathbf{C}_T \cdot \mathbf{Q} \tag{6.40}$$

for arbitrary rotations $\mathbf{Q}$. As a consequence, the tangential material stiffness matrix $\mathbf{C}_T$ has to follow a form like Eq. (6.22), which allows only for two independent coefficients.

Materials initially isotropic may become anisotropic in higher loading levels. In the case of concrete a *load-induced anisotropy* especially arises with cracking whereby the direction normal to a crack has a reduced capacity to transmit tensile stresses while stiffness and strength may remain unaffected in the direction of a crack (Figure 3.3a).

Orthotropic forms may be used to model a load-induced anisotropy due to cracking. The tangential material stiffness matrix $\mathbf{C}_T$ then has to obey to a form like Eq. (6.25) or Eq. (6.34) in the case of plane stress and shear isotropy. The respective matrix coefficients may depend on stress, strain, and loading history according to Eq. (6.38). The orthotropic tangential material flexibility $\mathbf{D}_T$ for 3D states gets a form according to Eq. (6.26) with varying coefficients. Corresponding forms are derived in Section 7.4 within the framework of 2D smeared crack models (Section 3.5).

6.4.2 Principal Stress Space and Isotropic Strength

Stress limit states mark the other end compared to initial states. They describe the *strength* of materials. For initially isotropic materials like concrete, such *stress limit states* are described by an isotropic *strength condition*

$$g(I_1, J_2, J_3) = 0 \tag{6.41}$$

using stress invariants I_1, J_2, J_3 derived from principal stress values $\sigma_1, \sigma_2, \sigma_3$ by Eq. (6.19). Stress states with $g(I_1, J_2, J_3) \leq 0$ are admissible; states $g(I_1, J_2, J_3) > 0$ cannot be sustained. This has some implications.

- The orientation of principal stress directions relative to material directions (Section 6.3) has no influence on the strength condition.

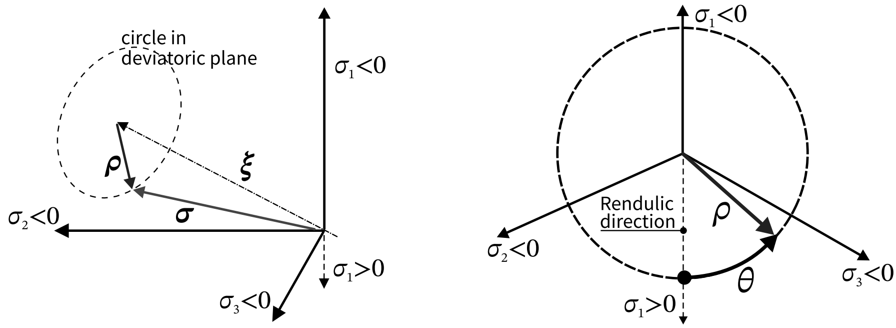

Figure 6.4 (a) Hydrostatic length and deviatoric plane. (b) Deviatoric length and Lode angle in the deviatoric plane.

- Furthermore, an exchange of principal stress values (Section 6.2.3) does not have any influence on the strength condition either.
- Admissible forms for equivalent functions $f(\sigma_1, \sigma_2, \sigma_3)$ derived from $g(I_1, J_2, J_3)$ by using Eq. (6.19) are constrained by the inherent structure of the invariants.

We assume the admissible forms $f(\sigma_1, \sigma_2, \sigma_3)$ for the following.

The stress–strain behaviour described by Eq. (6.37) is sometimes separated from the strength limit states described by $f(\sigma_1, \sigma_2, \sigma_3)$, and both are treated independently. To have a consistent material description the integration of stresses $\dot{\boldsymbol{\sigma}}$ from Eq. (6.37) during the loading history driven by a time t should not lead to stress states violating the strength condition Eq. (6.41). The elasto-plastic material models described in Section 6.5, the damage models described in Section 6.6, or the microplane models described in Section 6.8 combine stress–strain relations and strength in such a way that the consistency of the material description is ensured.

An isotropic strength condition generally becomes active with one predominant principal stress component. Let us assume that σ_1 activates the tensile strength in the 1-direction. The respective material point is generally not considered to fail in every aspect. A utilisation of strength in the remaining directions is still allowed in the following loading history. Thus, e.g. a load-induced anisotropy – tensile strength is reached in one direction, while compressive strength is utilised in orthogonal directions – may be combined with an isotropic strength condition.

*Iso*tropic strength conditions basically do not exclude *aniso*tropic stress–strain relations.

Such isotropic strength conditions $f(\sigma_1, \sigma_2, \sigma_3)$ are used for concrete and will be considered in the following.

Principal stress values span a triaxial Cartesian coordinate system (→ principal stress space), and the corresponding stress state is given by a vector. This has the following significant elements, see also Figure 6.4:

- The hydrostatic axis as a space diagonal with a direction $\mathbf{n}_\xi = \begin{pmatrix}1 & 1 & 1\end{pmatrix}^T/\sqrt{3}$. A direction is a vector of length 1 by definition.
- The projection of a stress vector $\boldsymbol{\sigma} = \begin{pmatrix}\sigma_1 & \sigma_2 & \sigma_3\end{pmatrix}^T$ on the hydrostatic axis: $\boldsymbol{\xi} = \xi\begin{pmatrix}1 & 1 & 1\end{pmatrix}^T/\sqrt{3}$ with hydrostatic length $\xi = (\sigma_1 + \sigma_2 + \sigma_3)/\sqrt{3}$.
- The deviatoric plane with origin at $\boldsymbol{\xi}$ and a normal $\mathbf{n}_\xi$. It is spanned by all vectors starting in $\boldsymbol{\xi}$ with zero hydrostatic length ξ.
- The projection of a stress vector $\boldsymbol{\sigma} = \begin{pmatrix}\sigma_1 & \sigma_2 & \sigma_3\end{pmatrix}^T$ on its deviatoric plane

$$\boldsymbol{\rho} = \boldsymbol{\sigma} - \boldsymbol{\xi} = \frac{1}{3}\begin{pmatrix}2\sigma_1 - \sigma_2 - \sigma_3 \\ -\sigma_1 + 2\sigma_2 - \sigma_3 \\ -\sigma_1 - \sigma_2 + 2\sigma_3\end{pmatrix} \tag{6.42}$$

  with $\rho_1 + \rho_2 + \rho_3 = 0$.
- The projection of the particular vector $\boldsymbol{\sigma} = \begin{pmatrix}1 & 0 & 0\end{pmatrix}^T$ on the deviatoric plane according to Eq. (6.42): $\boldsymbol{\rho}_1 = 2/3\begin{pmatrix}1 & -\frac{1}{2} & -\frac{1}{2}\end{pmatrix}^T$. It has a direction $\overline{\boldsymbol{\rho}}_1 = \sqrt{2/3}\begin{pmatrix}1 & -\frac{1}{2} & -\frac{1}{2}\end{pmatrix}^T$ called the Rendulic direction in the following.

An isotropic strength condition like Eq. (6.41) forms a *strength surface* in the principal stress space and defines triaxial strength. A stress vector and, in particular, a point on this surface can be described by *Haigh–Westergaard coordinates* with the following components:

- The *hydrostatic length* ξ is already introduced as length of the stress vector on the hydrostatic axis

$$\xi = \frac{1}{\sqrt{3}}(\sigma_1 + \sigma_2 + \sigma_3) = \frac{I_1}{\sqrt{3}} \quad \rightarrow \quad I_1 = \sqrt{3}\,\xi \tag{6.43}$$

- The *deviatoric length* ρ results from the length of the vector $\boldsymbol{\rho}$ from Eq. (6.42). This leads to the second invariant of the stress deviator (Eq. (6.19))

$$\rho = |\boldsymbol{\rho}| = \sqrt{2J_2} \quad \rightarrow \quad J_2 = \frac{\rho^2}{2} \tag{6.44}$$

- The *Lode angle* θ spans between the Rendulic direction and deviatoric direction

$$\cos\theta = \frac{1}{\rho}\boldsymbol{\rho}\cdot\overline{\boldsymbol{\rho}}_1 \tag{6.45}$$

  A common alternative of this formulation is given by

$$\cos 3\theta = 4\cos^3\theta - 3\cos\theta = \frac{3\sqrt{3}}{2}\frac{J_3}{\sqrt{J_2^3}} \tag{6.46}$$

  with the second and third invariants J_2, J_3 of the stress deviator (Eq. (6.19)). Equation (6.46) yields one solution in the range $0° \le \theta \le 60°$. But this is not a restriction, as any interchanging of $\sigma_1, \sigma_2, \sigma_3$ is equivalent; see the remarks following Eq. (6.41).

A convention

$$\sigma_1 \geq \sigma_2 \geq \sigma_3 \tag{6.47}$$

(signed!) is generally used without loss of generality with respect to isotropic strength. Thus, a state of stress is uniquely determined by ξ, ρ and, finally, θ in the range $0 \leq \theta \leq 60°$.

6.4.3 Strength of Concrete

The strength of solid materials is determined experimentally with specimens of at least the size of an representative volume element (RVE) (Section 6.1.1). Cylindrical specimens are often used for concrete. A typical experimental set-up is shown in Figure 6.5 with the *triaxial cell*.

It allows applying longitudinal and radial pressure independently from another. The radial pressure is connected with a circumferential pressure of the same value to establish equilibrium. Both form the confining pressure. A first principal stress directly corresponds to the longitudinal pressure; the confining pressure leads to the identical second and third principal stress. A test is started with identical longitudinal and confining pressures. After that, the longitudinal pressure is changed until it reaches an extremal value corresponding to strength. Such a set-up has the following locations in the principal stress space:

- The *compressive meridian* with $\sigma_1 = \sigma_2 > \sigma_3$ (signed): a cylindrical specimen with compression $\sigma_3 < 0$ in the longitudinal direction and circumferential confining pressure $\sigma_1 = \sigma_2 < 0$, $|\sigma_1| < |\sigma_3|$. Equation (6.19) yields $J_2 = (\sigma_1 - \sigma_3)^2/3$ and $J_3 = -2(\sigma_1 - \sigma_3)^3/27$ and Eq. (6.46) $\cos 3\theta = -1$ or $\theta = 60°$.
- The *tensile meridian* with $\sigma_1 > \sigma_2 = \sigma_3$ (signed): a cylindrical specimen with circumferential confining pressure $\sigma_2 = \sigma_3 < 0$ and a longitudinal compression $\sigma_1 < 0$, $|\sigma_1| < |\sigma_3|$. Equation (6.19) yields $J_2 = (\sigma_1 - \sigma_3)^2/3$ and $J_3 = 2(\sigma_1 - \sigma_3)^3/27$ and Eq. (6.46) $\cos 3\theta = 1$ or $\theta = 0°$.

The compressive and tensile meridians form particular curves within the strength surface as is shown in Figure 6.6. They are determined as the intersection of the strength surface with the deviatoric planes with Lode angles $\theta = 60°$ and $\theta = 0°$, re-

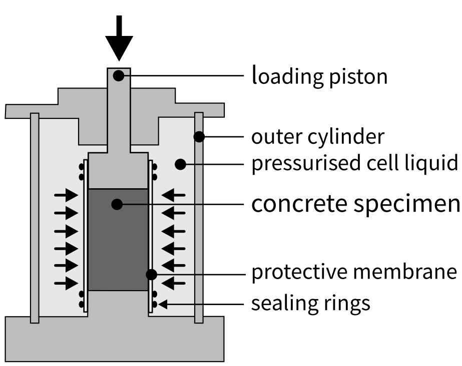

Figure 6.5 Triaxial cell.

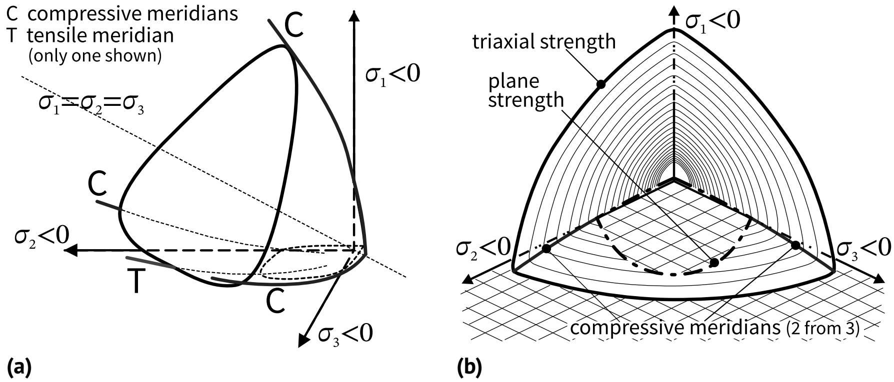

Figure 6.6 Strength surfaces. (a) General view direction. (b) Pressure axis view direction.

spectively. Strength surfaces of concrete themselves form a smoothed, curved tetrahedron (Figure 6.6). Its tip is located in the positive octant ($\sigma_1 > 0, \sigma_2 > 0, \sigma_3 > 0$) near the origin. The origin indicates the triaxial tensile strength. The strength surface opens in the negative octant ($\sigma_1 < 0, \sigma_2 < 0, \sigma_3 < 0$) and can be specified as follows:

- Many experimental data exist for the compressive and the tensile meridians due to the relatively simple triaxial cell set-up (Figure 6.5). Both meridians are slightly curved. The tensile meridian falls below the compressive meridian, if both are sketched in a plane.
- The range between compressive and tensile meridians with a Lode angle $0° \leq \theta \leq 60°$ is sufficient to describe the whole strength surface. This section replicates for the remaining range full range of θ due to the isotropic strength condition; see the remarks following Eq. (6.41). This also replicates the meridians.
- The range $0° \leq \theta \leq 60°$ has three different principal stresses, which cannot be realised with the conventional triaxial cell according to Figure 6.5. True triaxial cells are required with a much higher experimental effort, and experimental data are rare in this range (Hampel et al. 2009).
- Strength 'increases' under hydrostatic pressure. Or more precisely, the admissible deviatoric length increases with increasing pressure for a certain range of pressures. This also depends on the Lode angle.
- The deviatoric concrete strength under very high pressures is not really known yet. From a theoretical point of view, there is no strength limit for a pure pressure. Practically, pure pressure is not reachable in experimental set-ups. Small deviatoric parts cannot be avoided.
- The tensile strength in multi-axial tension does not significantly differ from uniaxial tensile strength. Thus, it should be possible to reach the uniaxial tensile strength in three directions simultaneously. But this has not yet been proved experimentally up to now.

A stress–strain relation has to be defined for all states within the strength surface. This may be assumed as isotropic linear elastic initially and become increasingly nonlinear when approaching the strength surface. Basic approaches to describe nonlinear material behaviour are given with elasto-plasticity described in Section 6.5, damage described in Section 6.6, and microplane described in Section 6.8.

A selection of widely referenced formulations for the strength surface of concrete is given in the following.

- The strength surface of *Ottosen* (Ottosen 1977)

$$f = a\,\frac{J_2}{f_c^2} + \lambda\,\frac{\sqrt{J_2}}{f_c} + b\,\frac{I_1}{f_c} - 1 = 0 \tag{6.48}$$

  with the uniaxial compression strength f_c (unsigned), constants a, b, and

$$\begin{aligned} \lambda &= k_1\,\cos\left[\frac{1}{3}\arccos(k_2\cos 3\theta)\right], && \text{for } \cos 3\theta \geq 0 \\ \lambda &= k_1\,\cos\left[\frac{\pi}{3} - \frac{1}{3}\arccos(-k_2\cos 3\theta)\right], && \text{for } \cos 3\theta \leq 0 \end{aligned} \tag{6.49}$$

  with further constants k_1, k_2. The four material constants a, b, k_1, k_2 are determined from the tensile strength f_{ct}, the biaxial strength, and points on the compressive meridian.
- The strength surface of *Hsieh–Ting–Chen* (Hsieh et al. 1982)

$$f = a\,\frac{J_2}{f_c^2} + b\,\frac{\sqrt{J_2}}{f_c} + c\,\frac{\sigma_1}{f_c} + d\,\frac{I_1}{f_c} - 1 = 0 \tag{6.50}$$

  with constants a, b, c, d and the largest principal stress σ_1. This is rewritten as

$$f = \overline{a}\left(\frac{\rho}{f_c}\right)^2 + \left(\overline{b}\cos\theta + \overline{c}\right)\frac{\rho}{f_c} + \overline{d}\,\frac{\xi}{f_c} - 1 = 0 \tag{6.51}$$

  with the hydrostatic length ξ (Eq. (6.43)), the deviatoric length ρ (Eq. (6.44)), and Lode angle θ (Eq. (6.46)). Hence, the largest principal stress σ_1 is replaced by invariants.
- The strength surface of *Willam/Warnke* (Willam and Warnke (1975), Chen and Saleeb (1994, Section 5.5)).

$$\overline{\rho} = \frac{2\rho_c(\rho_c^2 - \rho_t^2)\cos\theta + \rho_c(2\rho_t - \rho_c)\sqrt{4(\rho_c^2 - \rho_t^2)\cos^2\theta + 5\rho_t^2 - 4\rho_t\rho_c}}{4(\rho_c^2 - \rho_t^2)\cos^2\theta + (\rho_c - 2\rho_t)^2} \tag{6.52}$$

  with

$$\overline{\xi} = a_0 + a_1\,\rho_t + a_2\,\rho_t^2\,, \qquad \overline{\xi} = b_0 + b_1\,\rho_c + b_2\,\rho_c^2 \tag{6.53}$$

  and $\overline{\xi} = \xi/f_c$, $\overline{\rho} = \rho/f_c$. The parameters ρ_t describe the normalised tensile meridian, i.e. $\theta = 0°$ and ρ_c the normalised compressive meridian, i.e. $\theta = 60°$. The parameters $a_0, a_1, a_2, b_0, b_1, b_2$ are material constants. As the compressive and